Raman lidar system for the measurement of water vapor and aerosols in the Earth's atmosphere

D. N. Whiteman, S. H. Melfi, and R. A. Ferrare

A nighttime operating Raman lidar system that is designed for the measurement of high vertical and temporal resolution profiles of the water vapor mixing ratio and the aerosol backscattering ratio is described. The theory of the measurements is presented. Particular attention is given to operational problems that have been solved during the development of the system. Data are presented from Sept. 1987 and described in their meteorological context.

Key words: Raman, lidar, water vapor, aerosols.

I. Introduction

Water vapor and aerosols are two interesting atmospheric parameters that are accessible to remove measurement. The water vapor mixing ratio, which is defined as the mass of water vapor divided by the mass of dry air in a given volume, is conserved in atmospheric processes that do not involve evaporation or condensation. Thus the mixing ratio is useful as a tracer of air parcels and in understanding energy transport within the atmosphere. Increased knowledge of water vapor concentration and motion can lead to a better understanding of cloud formation, convective storm development, and the hydrological cycle. Aerosol measurements, on the other hand, are important in a number of research areas, such as the retrieval of atmospheric and surface characteristics from satellite data and the impact of aerosols on climate and air pollution studies.

Lidar is a well-established technique for measuring both water vapor and aerosols. The early work of Cooney[1] and Melfi *et al.*,[2] in the late 1960's demonstrated the technique of Raman spectroscopy in the measurement of tropospheric water vapor. Later Pourney *et al.*[3] demonstrated the possibility of producing imagery that depicts the temporal evolution of the water vapor mixing ratio profile. In 1985 Melfi and Whiteman[4] extended this capability in both spatial and temporal resolution. Vaughan *et al.*[5] have since taken mixing ratio measurements up to the tropopause, and Melfi *et al.*[6] have used Raman lidar to record the passage of frontal systems. These measurements have demonstrated that Raman lidar can be used as a meteorological research tool that is unique in its ability to capture the spatial and temporal evolution of water vapor in the lower atmosphere. On the other hand, aerosol measurements were the first application of lidar in the early 1960's. For example, the semipermanent stratospheric aerosol layer that was first measured by Junge and Manson[7] by using balloons was later measured by using lidar.[8] More recently the measurement of aerosol concentration has been used to discern cloud top heights[9] and the height of the boundary layer and its variation.[10]

This paper describes a Raman lidar system that is capable of measuring both the water vapor mixing ratio and the aerosol backscattering ratio with sufficient reliability to allow essentially continuous nighttime operation. The method that is employed in the measurements is described, and the theory is discussed next. The equipment is then detailed. Emphasis is given to the solutions of several operational problems that can limit lidar measurements of this kind. The various methods of analysis are then discussed, and the results are presented from recent intensive measurement programs that were conducted in Greenbelt, Md., on Cape Cod, Mass., and at Wallops Island, Va.

II. Method

The experiment is based on a frequency-tripled Nd:YAG laser transmitter, an optical telescope receiver,

D. N. Whiteman is with the Laboratory for Terrestrial Physics, NASA Goddard Space Flight Center, Code 924, Greenbelt, Maryland 20771. S. H. Melfi and R. A. Ferrare are with the Laboratory for Atmospheres, NASA Goddard Space Flight Center, Code 917, Greenbelt, Maryland 20771. R. A. Ferrare is also with the Universities Space Research Association.

Received 29 May 1990.
0003-6935/92/163068-15$05.00/0.

and various signal-processing and data-acquisition electronics. A pulsed laser beam is directed vertically through the atmosphere. As the beam propagates upward, it interacts with air molecules and aerosols. The backscattered radiation caused by Raman, Rayleigh, and Mie processes is detected and recorded as a function of height. These return signals are analyzed to determine the vertical profiles of the water vapor mixing and aerosol backscattering ratios. The details of the equipment are described after the relevant theory is reviewed.

III. Theory

Raman scattering is a weak molecular-scattering process that is characterized by a shift in wavelength of the scattered beam of light relative to the incident one. The shift can be to either longer or shorter wavelengths. The Raman shift toward a longer wavelength is much more likely at typical atmospheric temperatures and is known as the Stokes component of Raman scattering. This is the type of Raman scattering that is used in the present experiment. Some of the energy of the incident photon is converted to rotational–vibrational energy within the molecule that results in the wavelength shift of the scattered photon. The amount of this shift depends on the rotational–vibrational energy level structure of the particular molecule being considered and is unique to it. For a photon of certain incident wavelength therefore, the shifted wavelength of the scattered photon is a signature of the molecule doing the scattering.[11]

The rotational–vibrational spectrum of N_2 corresponding to the Raman vibrational transition $\nu = 0$–1 is shifted by 2330.7 cm^{-1} from the exciting frequency.[12] When excited at a wavelength of 354.7 nm from a tripled Nd:YAG laser, the center of the shifted spectrum is at 386.7 nm. The ν_1 Raman vibrational spectrum of water vapor is shifted by approximately 3652 cm^{-1} from the exciting line.[13–15] In response to the 354.7-nm radiation the center of the water vapor Raman spectrum is thus ~407.5 nm. The return signal at the laser wavelength (354.7 nm) is produced by Rayleigh and rotational Raman scattering from molecules and Mie scattering from aerosol particles.

The backscattered signals from the Rayleigh–Mie channel at 354.7 nm, the Raman nitrogen channel at 386.7 nm, and the Raman water vapor channel at 407.5 nm are given by the following three equations, respectively:

$$S_{\lambda_0}(z) = \frac{k_{\lambda_0}}{z^2}[\sigma_R(\pi)n_R(z) + \sigma_A(\pi)n_A(z)]q^2(\lambda_0, z_0, z), \quad (1)$$

$$S_{N,H}(z) = \frac{k_N}{z^2}\sigma_{N,H}(\pi)n_{N,H}(z)q(\lambda_0, z_0, z)q(\lambda_{N,H}, z_0, z), \quad (2)$$

$$S_{N,H}(z) = \frac{k_H}{z^2}\sigma_{N,H}(\pi)n_{N,H}(z)q(\lambda_0, z_0, z)q(\lambda_{N,H}, z_0, z), \quad (3)$$

where

$S_x(z)$ is the return signal caused by channel x;
$\sigma_x(\pi)$ is the backscatter cross section for species x whether caused by Raman, Rayleigh, or Mie scattering;
$n_x(z)$ is the number density for species x as a function of height z;
$q(\lambda_x, z_0, z)$ is the atmospheric transmissivity from the lidar at height z_0 to height z at wavelength λ_x and is equal to

$$\exp\left(-\int_{z_0}^{z}\alpha_{\lambda_z}(z')dz'\right),$$

where

α_{λ_x} is the volume extinction coefficient at wavelength λ_x,
k_x is a proportionality constant for channel x that accounts for the system optical efficiency, the telescope receiver area, the photomultiplier tube (PMT) spectral efficiency, and the laser output energy;
λ_0 refers to the output laser wavelength (354.7 nm).

The subscript x represents R, which refers to Rayleigh parameters; A, which refers to Mie (aerosol) parameters; and N, which refers to the Raman nitrogen parameters, or and H, which refers to the Raman water vapor parameters.

A. Water Vapor Mixing Ratio

The water vapor mixing ratio is the mass of water vapor divided by the mass of dry air in a given volume. As a function of height the water vapor mixing ratio can be expressed as

$$w(z) = \frac{n_H(z)}{n_{dry}(z)}\frac{M_H}{M_{dry}}, \quad (4)$$

where M refers to the respective molecular weight. Nitrogen is in constant proportion to dry air at the heights over which these measurements are made, and thus the Raman nitrogen return signal is used as a measure of the mass of dry air. The mixing ratio then can be determined from the lidar data by using the Raman-shifted signals from water vapor and nitrogen. By using Eqs. (2) and (3) we can express the mixing ratio w as

$$w(z) = C_w\Delta_q^w(z_0, z)\frac{S_H(z)}{S_N(z)}, \quad (5)$$

where

$$C_w = \frac{k_N}{k_H}\frac{\sigma_N(\pi)}{\sigma_H(\pi)}\frac{M_H}{M_{dry}}\frac{n_N}{n_{dry}}$$

is the system calibration constant for the water vapor mixing ratio measurement and

$$\Delta_q^w(z_0, z) = \frac{q(\lambda_N, z_0, z)}{q(\lambda_H, z_0, z)}$$

is the transmission correction function for the water vapor mixing ratio calculation that is now discussed.

From Eq. (5) the mixing ratio is seen to be proportional to the ratio of Raman lidar signals for water vapor and nitrogen with the exception of the transmission correction term $\Delta_q^w(z_0, z)$. The transmissivities $q(\lambda_N, z_0, z)$ and $q(\lambda_H, z_0, z)$ differ primarily as a result of the λ^{-4} dependence of Rayleigh scattering by air molecules. The difference in transmission between the two wavelengths λ_N and λ_H as a result of Rayleigh scattering is easily accounted for and is ~5% between 0 and 7 km. An additional correction is needed for the wavelength dependence of Mie scattering by aerosols. A λ^{-1} wavelength dependence in the aerosol extinction coefficients is used within the wavelength range of the experiment (354.7–407.5 nm).[16] By using the vertical distributions of aerosols given by Shettle and Fenn,[16] the differential transmission correction curve $\Delta_q^w(z_0, z)$ has been calculated and is shown as the family of curves on the left-hand side of Fig. 1. The curve for an aerosol optical thickness of zero represents the differential transmission caused by Rayleigh scattering alone and is shown by the solid line. The 5% effect between the surface and 7 km is clearly seen. A value of aerosol optical thickness $\tau_A = 1$ corresponds to quite hazy conditions and produces an additional 5% correction between 0 and 7 km. The actual amount of aerosol correction that is used is between 0% and 5% and is estimated from the lidar aerosol data. Once the differential transmission is accounted for, the constant C is determined by calibration with respect to a simultaneous radiosonde. This is discussed further in Section VII. Absorption by ozone and other trace gases is negligible at these wavelengths.

The approximation is used that the Raman backscatter cross sections are constant over the temperature changes that are expected in the atmosphere. At a given wavelength within the rotational fine structure, the Raman backscatter cross sections are highly temperature dependent. However, the integrated total of the Raman spectrum is considered to be independent of temperature because essentially all the molecules are at the vibrational ground state at typical atmospheric temperatures.[13] If the interference filter that is used to select the Raman scattering covers the complete spectrum, there should be no temperature sensitivity to the measured backscatter for the purposes of these atmospheric measurements.

In the case of the Raman nitrogen channel, the filter used is centered approximately 1 nm from the peak of the Q branch at 386.7 nm (see Table I). Approximately 3% of the intensity of the S branch is thereby excluded by the filter. The S branch of the backscatter is approximately 6% of the total vibrational plus rotational Raman backscatter. The excluded portion of the S branch is therefore less than 0.2% of the total backscatter. The temperature sensitivity of this excluded portion is insignificant. It should be noted here that the light passing through the interference filters is highly collimated. The most extreme rays diverge from the parallel by at most 2 deg. This introduces a shift in the center of the passband of the filter of ~1 Å for these extreme rays. Given the nominal 5–6-nm bandwidths of the filters, the effect of this center shift is negligible.

In the case of the Raman water vapor backscatter, the only significant contribution to the Raman spectrum is made by the Q branch.[13,14] It spans a region of approximately 20 cm^{-1} with a band origin at a shift of 3657.5 cm^{-1}. In response to 354.7-nm radiation, this corresponds to a band of 0.3-nm width centered at 407.5 nm, which is completely covered by the water vapor filter (see Table I). Thus there should be no temperature sensitivity to the water vapor return signal.

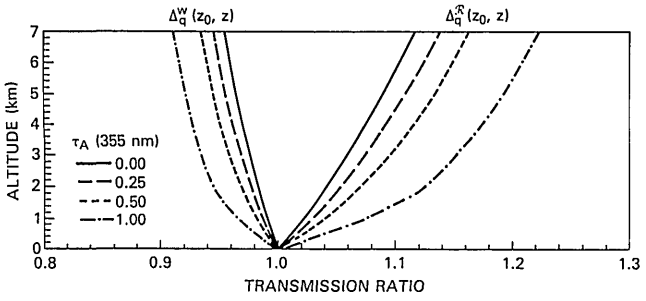

Fig. 1. Transmission correction curves for the water vapor mixing ratio and the aerosol backscattering ratio calculations as shown in Eqs. (5) and (7). The family of curves on the left represents the differential transmission correction that is required in the water vapor mixing ratio calculation for a range of optical depths. The corrections range from between 5 and 9% depending on the amount of aerosols that are present for a transmission path from the ground up to 7 km. The curve corresponding to $\tau_A = 0.00$ represents the correction that is required when no aerosols are present, while the $\tau_A = 1.00$ curve represents a quite hazy condition. In practice the correction is between these two limits. The family of curves on the right represents the correction that is required in the aerosol backscattering ratio calculation where the range of correction is between 11 and 22%.

B. Aerosol Backscattering Ratio

The backscatter at the laser wavelength is caused by Rayleigh scattering from air molecules and Mie scattering from aerosol particles. The aerosol backscattering ratio is used to quantify the ratio of aerosol to molecular scattering. It is defined as the ratio of the volume backscatter coefficients β or the total Rayleigh–Mie signal to the Rayleigh backscatter alone.[17]

$$\mathcal{R}(\lambda_0, z) = \frac{\beta_R(z) + \beta_A(z)}{\beta_R(z)} = 1 + \frac{\beta_A(z)}{\beta_R(z)}, \tag{6}$$

where

$$\beta_R(z) = \sigma_R(\pi) n_R(z),$$

$$\beta_A(z) = \sigma_A(\pi) n_A(z),$$

where the parameters that are used are as described in Eqs. (1)–(3). Because of the wavelength dependence of the backscatter cross sections that are used in Eq. (6), $\mathcal{R}$ is found to vary depending on the wavelength of the exciting laser. In our case the Raman nitrogen return signal is used as a measure-

Table I. Interference Filter Characteristics and Components

	Raman Nitrogen	Raman Water Vapor	Rayleigh–Mie
Center wavelength (nm)	385.5	407.8	354.8
Bandwidth (nm full width at half-maximum)	4.5	4.9	6.5
Peak transmission (%)	25	26	28
Filter components	3-mm Corning 751 Five vacuum coatings	2-mm Schott BG 25 3-mm Schott BG 39 1-mm Schott GG 400 Three vacuum coatings	4.5-mm Schott UG 11 Two vacuum coatings

ment of the pure Rayleigh return, and the return signal at the laser wavelength is a measurement of both Rayleigh and Mie scattering. It should be noted at this point that the return signal at the laser wavelength also contains a signal caused by rotational Raman scattering from the various atmospheric constituents. As in the case of the Raman-shifted spectrum, the integrated total of the rotational Raman spectrum can be considered to be constant at atmospheric temperatures. Once again the spectrum is completely covered by the interference filter that we used. The result of this is that the backscatter coefficient σ_R that is used above is increased by $\sim 5\%$ over the pure Rayleigh coefficient.[11] The terms in Eq. (6) that refer to the Rayleigh–Mie backscatter actually include this additional backscattering.

It can be seen from Eq. (6) that the aerosol backscattering ratio will equal unity in a region of atmosphere that is free of aerosols and will exceed unity where aerosols are present. The aerosol backscattering ratio can be expressed in terms of the lidar signals by using Eqs. (1) and (2) as

$$\mathscr{R}(\lambda_0, z) = C_{\mathscr{R}} \Delta_q^{\mathscr{R}}(z_0, z) \frac{S_{\lambda_0}(z)}{S_N(z)}, \tag{7}$$

where

$$C_{\mathscr{R}} = \frac{k_N}{k_{\lambda_0}} \frac{\sigma_N(\pi) n_N(z)}{\sigma_R(\pi) n_R(z)}$$

is the system calibration constant for the aerosol backscattering ratio measurement and

$$\Delta_q^{\mathscr{R}}(z_0, z) = \frac{q(\lambda_N, z_0, z)}{q(\lambda_A, z_0, z)}$$

is the transmission correction function for the aerosol backscattering ratio case.

Equation (7) indicates that once the differential transmission correction has been applied, the ratio of the return signals from the Rayleigh–Mie scattering and Raman nitrogen scattering is proportional to the aerosol backscattering ratio and can thus be normalized to unity in an aerosol-free region. In aerosol-laden regions the ratio will exceed unity. The same assumptions regarding aerosols that were made in the water vapor case are made here as well. For this wavelength pair of $\lambda_N = 386.7$ nm and $\lambda_A = 354.7$ nm, the transmission difference is slightly larger than in the water vapor case because the wavelength separation is greater and the wavelengths are shorter. Therefore in this case the transmission difference between these heights caused by Rayleigh scattering between 0 and 7 km is $\sim 12\%$, while the additional difference caused by Mie scattering between these altitudes is up to 11% depending on the amount of haze. The correction curves for the aerosol case are shown as the family of curves on the right-hand side of Fig. 1.

By definition Eq. (6) equals one at a height z^*, which is free of aerosols. This can be used to normalize the lidar signals in terms of known quantities. The value of Eq. (7) at the aerosol-free height of z^* is used to normalize the aerosol backscattering ratio to unity. Dividing Eq. (7) by this normalization value yields

$$\mathscr{R}(\lambda_0, z) = \frac{\Delta_q^{\mathscr{R}}(z)}{\Delta_q^{\mathscr{R}}(z^*)} \frac{S_A(z)/S_N(z)}{S_A(z^*)/S_N(z^*)} = \Delta_q^{\mathscr{R}}(z, z^*) \frac{S_A(z)/S_N(z)}{S_A(z^*)/S_N(z^*)}, \tag{8}$$

where z^* is a height at which all the backscatter at the laser wavelength is caused by air molecules. This height is determined operationally by finding the minimum of the lidar profile over the altitude range of 4–7 km, as discussed in more detail in Section VII. Note that this normalization technique causes all the system parameters to cancel out and leaves only the differential transmission to be corrected for. In addition the assumption is made that the backscatter cross sections are constant with respect to temperature. As described in the water vapor case there is at most a 0.2% error in this assumption in the case of the Raman nitrogen data. For the aerosol channel the interference filter completely covers the rotational Raman lines, and thus the backscatter is insensitive to temperature.

IV. Equipment

All the lidar equipment is housed in a 13.4-m (44-ft) environmentally controlled mobile trailer. The equipment is discussed in the two broad categories of optical components and data system.

A. Optical Components

The laser is a Quanta-Ray DCR1A Nd:YAG that is operated in the frequency-tripled mode with an output wavelength of 354.7 nm. The housing for the KD*P frequency-multiplying crystals is temperature

controlled, which provides excellent long-term output power stability. We have found that for periods of operation in excess of 10 h, the laser power decreases from its maximum of 150 mJ/pulse by no more than 10%. The standard deviation of the laser output energy is ~15 mJ. A system diagram is shown in Fig. 2. The telescope is a 0.75-m, $f/4.8$ Dall–Kirkham design with a variable field stop that is adjustable from 0.3- to 5-mrad field of view. All reflective surfaces of the telescope are coated with aluminum and an overcoat of SiO_x so that the reflection is maximized in the 300–408-nm wavelength range. The output laser beam and the telescope are aligned parallel and pointed vertically through a hatch in the roof of the trailer. The system has provisions that allow the laser to be transmitted either coaxially or biaxially with respect to the axis of the telescope. Dichroic beam splitters that are manufactured by CV I Lasers separate the light that is collected by the telescope into three paths. Interference filters from Barr Associates select the desired wavelength band for each photomultiplier channel. The characteristics of these filters are given in Table I. The detectors are Amperex XP2020 photomultiplier tubes that offer a 12-stage linear focus dynode chain with a usable gain of 3×10^7. The tubes are normally operated at fixed voltages between 2200 and 2400 V.

The interference filters in the Raman-shifted channels must provide a high degree of blocking at the laser wavelength. The Raman-shifted return signals are 3–4 orders of magnitude less than the Rayleigh–Mie return. This Rayleigh–Mie return must be completely rejected. The Raman channel interference filters were designed so that the transmission would be 10–12 orders of magnitude less at the laser wavelength than at the Raman-shifted wavelengths, offering essentially complete rejection of the Rayleigh–Mie return. It was not possible to measure this degree of blocking directly. Instead the transmission of each of the individual components was measured by the manufacturer and shown to exceed the design requirement.

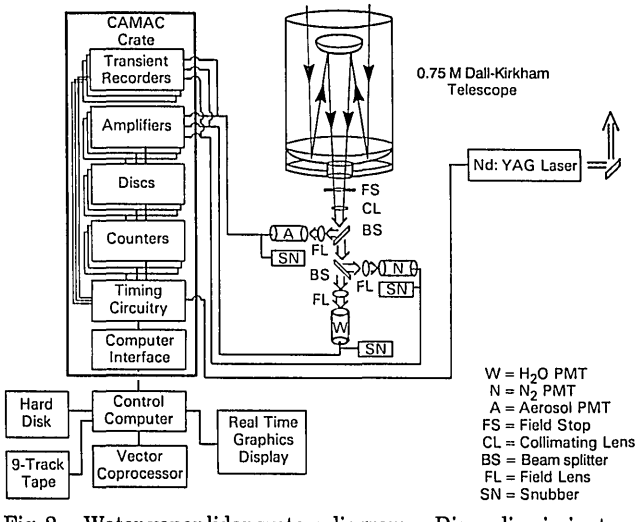

Fig. 2. Water vapor lidar system diagram: Discs, discriminators.

This out-of-band blocking requirement in the filter for the Rayleigh–Mie channel is less than for the Raman channels because the interfering signals are much less intense than the direct Rayleigh–Mie return as noted. The out-of-band transmission of the filter in this channel is 6 orders of magnitude less than for the center wavelength (354.7 nm), offering essentially complete rejection of the relatively weak Raman signals (and any fluorescence at the laser wavelength).

As described in Ref. 4 an operational check on light rejection is conducted by analyzing the Raman returns when a low cloud is present. The strong Rayleigh–Mie backscatter signals from both liquid water and ice clouds were found experimentally to be totally absent in the Raman channels.

B. Data System

The data system consists of a 20-MHz Digital Equipment Corporation LSI-11/73 computer that runs the TSX+ operating system. A Mercury Systems ZIP 3216 vector coprocessor that is capable of 10 million instructions per second is also installed in the computer backplane. The Q bus of the LSI is interfaced to a Standard Engineering computer automated measurement and control (CAMAC) crate by using a Caminton DR11-WA+ block mode direct access memory (DMA) module and a DSP CC-DR11 DMA crate controller. The CAMAC crate houses the data-acquisition electronics.

We acquire data in both the analog-to-digital (A/D) and photon-counting (PC) modes. The A/D instruments are used for the extremely strong low-altitude return signals, while the PC instruments are used for the weaker returns from above approximately 2 km. The A/D data are acquired every 100 ns by using 8-bit, 32-MHz LeCroy TR8837F transient recorders. The PC data are acquired in 1-μs intervals by using Joerger Model S3 counters that offer a counting-rate capability in excess of 150 MHz. Before the pulses are counted they are amplified by a 200-MHz LeCroy Model 612 pulse amplifier and discriminated by a 300-MHz Phillips Scientific Model 708 discriminator. Amplifiers and electronic filters are not used in the A/D part of the data-acquisition system.

The data-acquisition sequence proceeds as follows. The computer initializes the vector coprocessor, and the data-acquisition electronics are set up to acquire data. The transient recorders acquire data that begin at a specified number of nanoseconds before the laser fires while the photon counters begin to take data when the laser fires. The computer enables a free-running oscillator to fire the laser. A photodiode detects the laser fire and sends an essentially coincident pulse that indicates that $t = t_0$ to a set of delay generators that were designed and built at the Goddard Space Flight Center. The photon counters receive a pulse coincident with t_0 and begin to acquire data in 1-μs bins. Data are acquired for 400 μs with the final 50 μs being used as a measurement of the PC background. These last 50 μs of data span an altitude

range of 52.5–60 km from which no atmospheric return is expected. The transient recorders receive a pulse that is delayed from the laser fire. This delayed pulse coupled with a pretrigger setting on the transient recorders is used to acquire data prior to the laser fire. These pretrigger data are used as a measure of the A/D background.

Once the data-acquisition instruments are finished acquiring data, the LSI reads the memory of the six instruments and performs a DMA transfer of the data to the LSI system memory. At this point the data are again transferred through the DMA to the memory of the ZIP 3216 coprocessor. (An error in the drivers for the ZIP prevented a direct transfer of the data from the CAMAC crate to the ZIP.) The ZIP then performs the 32-bit running sum and the sum of squares of the A/D data. For the PC data only the running sum is maintained by the coprocessor. The PC data are assumed to behave according to Poisson statistics: thus the variance equals the sum. However for the A/D data one must know the sum of the squares of the individual data points to calculate the variance.

Once the data are transferred to the ZIP coprocessor, the data-acquisition instruments are set up again for the next laser shot, and the cycle repeats at the 10-Hz repetition rate of the laser until data from the desired number of laser shots are acquired. At this point the oscillator that fires the laser is disabled, and the running sum and running sum of squares of the data are read out of the vector coprocessor and stored on a disk. The LSI then performs a background subtraction and range-squared correction for both the A/D data and PC data and plots uncalibrated line graphs of the water vapor mixing ratio and aerosol backscattering ratio on a graphics cathode-ray tube. After this off time of ~5 s, the laser fire sequence begins again. We tailor the data acquisition and graphing time so that the profiles begin 2 min apart. This results in each 2-min measurement being the accumulation of ~1140 laser shots. At the end of a night of work we typically have in excess of 200 profiles of the water vapor mixing ratio and aerosol backscattering ratio that is acquired on 2-min centers.

V. System Operations

In this section various topics that pertain to how we set up and operate the lidar are discussed. Solutions to several problems are also covered.

A. System Alignment

The alignment of the output laser beam with the field of view of the telescope is done with the aid of a Stanford Research SR400 photon counter. With this instrument it is possible to count photons in various altitude ranges easily. We typically measure the signal at two altitude ranges simultaneously with the telescope field of view stopped down to 1 mrad. After maximizing the signal at these altitude ranges the field of view is then opened up to the operational configuration of 3 mrad. The divergence of the laser is ~1 mrad. This alignment technique ensures that the beam is well centered in the field of view of the telescope and that, should any drift in the alignment occur, there will be a relatively large angle (1–2 mrad) over which the laser beam and the field of view of the telescope will still be fully overlapped.

B. Amplification and Bandpass Filtering in A/D Measurements

The extremely weak nature of the Raman-scattering process results in weak return signals. This places a great burden on signal acquisition systems. Typically these systems include A/D electronics. It is often necessary to amplify the photomultiplier tube (PMT) signal prior to digitization for the signal to cover a reasonable portion of the input range of the A/D recorders. In all the analog amplifiers that we tested small noise sources or nonlinearities present in the amplifier became dominant over the return signal at altitudes above ~4–5 km. Because of this we chose instead to use PMT's with gain high enough to produce signals that are capable of being digitized directly without the use of additional amplification. The XP2020 PMT's produce a peak analog signal between 50 and 300 mV (into the effective 25-Ω load), which alleviates the need for additional amplification. In addition to these amplifier problems we have also experienced difficulties in the use of bandpass filtering prior to digitization of the data.

In the early development of the Raman lidar system we attempted to make use of 3–5-MHz filters prior to digitizing the data. We tested several bandpass filters and found them all to exhibit some degree of overshoot when presented with the negative-going edge of a square pulse. This overshoot made them unsuitable for our needs. In addition we found that prefiltering the data can present problems when the average value of the return signal is very small.

The output of the PMT consists of sharp current spikes of only a few nanoseconds in duration. These spikes of current that are sent through a 25–50-Ω load resistance create voltage spikes of several tens of millivolts. The use of a bandwidth filter removes much of this natural variation of the signal and averages it out to some more constant value over the 100-ns digitization interval of the A/D recorder. An 8-bit digitizer with an input voltage range of 512 mV has a minimum digitization level of 2 mV. If the average value of the bandwidth-filtered signal drops below this 2-mV level, the digitizer registers a zero. Long-term averaging of the signal will not change this situation substantially. This limits the maximum range over which meaningful measurements can be made in the A/D mode to altitudes where the filtered signal is 2 mV or greater. If meaningful measurements are to be made when the average signal level is below 2 mV, bandwidth filtering cannot be used.

If instead the unfiltered output of the PMT is sent directly to the digitizer, then, in the low-signal regime being discussed, the digitizer is presented with voltage spikes that allow nonzero measurements to be

made. The digitizer will perform the averaging over many shots instead of the bandwidth-filter averaging on a shot-by-shot basis. This results in a better representation of the original signal. Alternate solutions would be to use a higher-resolution digitizer or photon counting (PC) for the higher-altitude return signal as in the present system.

Aliasing can be introduced if the sampling frequency is lower than the bandwidth of the signal. Aliasing must therefore be considered as a possible problem in the use of transient recorders without bandwidth filtering as described above. Aliasing causes high-frequency components of the signal to be misrepresented as lower-frequency ones in the data.[18] These spurious components in the data may have frequencies that fall anywhere within the range of the digitizer's measurement capability (frequencies that correspond to tens of meters to kilometers in spatial terms). However, the digital filtering of the data performed prior to any processing removes any small-scale components caused by aliasing. Also, any long-period components (corresponding to spatial scales of >150 m) in the A/D data can be checked against the PC record to see if they are spurious, the PC data being completely immune to aliasing. By performing this type of comparison over the several years that we have been making measurements in this fashion, we concluded that aliasing does not present a problem for data that are acquired in this manner.

C. Ground Loop and Background Noise Suppression

Because of the extremely weak nature of the Raman signals, noise levels of fractions of a millivolt, which for elastic backscatter lidar systems might be quite acceptable, can significantly reduce the signal to noise in a Raman lidar. This is primarily a problem when A/D recorders are used because PC circuitry includes a discriminator that can eliminate much of the low-level noise that is present in the system. The signals that the discriminator–counter circuitry are presented with consist of voltage spikes of typically many tens of millivolts, which are only a few nanoseconds in duration. The noise associated with these signals consists of spikes that are approximately an order of magnitude smaller. The dc equivalent of these noise spikes is usually a fraction of a millivolt and therefore quite negligible for the PC circuitry. On the other hand, this level of noise can be extremely detrimental to the A/D instruments.

For signals from an altitude of ~ 3 km, the typical return level is a few millivolts. By this altitude small noise sources of just a fraction of a millivolt can create a significant error in the A/D signal. It is therefore necessary to ensure that ground loops and rf pickup that can contribute to the background noise of the system be reduced to the microvolt level.

To minimize the ground loops in our system, all the various components of the data-acquisition system are isolated from the ground except for the CAMAC crate that is grounded through the ac power connection. The power ground for the laser is on a different circuit from that of the data system. The only connection between the laser and the data system is made through an optoisolator. This helps to isolate the noise that is associated with the laser discharge from the data-acquisition electronics.

In addition the connections between the PMT's and the transient recorders are permanently soldered together to minimize background noise caused by resistance variations in the connector contacts. Particularly in conditions of high relative humidity (RH), we found that these direct cable connections reduce our noise problems.

It is easy to test if the ground loops and rf pickup have been reduced to a negligible level. Data are acquired by operating the lidar in the operational configuration except when the laser output is blocked. A constant signal with time indicates that the background can be acceptably removed from the real lidar data. This test can be made even more stringent by processing these background data through a background subtraction and range-squaring routine as is normally done for the actual data.

D. A/D Instrument Setup

As a result primarily of fluctuations in laser output, the strength of the lidar return signal can vary greatly from shot to shot. When performing a running sum of many laser shots, one must take care to keep the signal well within the dynamic range of the data-acquisition instruments. This is primarily a problem in the early part of the return, where the signal is large. The data from the A/D instruments are used in the early part of the return as the photon counters are saturated until ~ 10 μs after the firing of the laser, which corresponds to an altitude of ~ 1.5 km. If too many of the individual recorded pulses that are used to make an average exceed the input range of the A/D recorders, significant clipping errors can be introduced.

To set the A/D instruments we establish a voltage level on the PMT, acquire a profile, and look at the average and the standard deviation of the data as a function of height. From this we can deduce on average what percentage of the individual recorded pulses exceeded the input range of the transient recorders and thus how we should adjust the voltage of the PMT's to maintain a better signal within the range of the instruments. The PMT voltages are adjusted so that the average signal is between 1.5 and 2 standard deviations below the maximum signal capability of the recorders.

E. Discriminator Setting

To implement PC the desired PMT signal pulses must be distinguished from background noise pulses. Real signal pulses originate at the photocathode caused by photon impacts on the photocathode and have thus been fully amplified. Smaller noise pulses can be thermally generated within the PMT at one or more of the dynodes and are not representative of photons that are incident on the photocathode. The threshold

on the discriminator must be set to allow the real signal counts to be recorded while rejecting as many of the noise counts as possible. The pulse height distribution of each Amperex XP2020 PMT has been determined by using a fast storage oscilloscope. The discrimination level is set by considering this pulse height information and the average level of the noise as seen on the scope. The ultimate verification that the discriminator setting is correct is provided by good agreement between the A/D and PC data sets. Examples of this comparison are presented in Section VII.

F. Photon-Counting Resolving Time

Data acquisition by the PC method is possible only when the photons are individually distinguishable. For our system the return signal level has decreased enough to allow this above an altitude of between 1 and 2 km, depending on the strength of the return signal. The highest count rates that we observe at these altitudes are typically 50–60 counts/μs. At these count rates there is a high probability that some pulses will have overlapped to the point of being indistinguishable from the discriminator–counter circuitry. Even at count rates that are well below the maximum of the system, there is a small but significant probability of photon overlap that produces a nonlinear response of the discriminator–counter circuitry to the detected PMT signal.

This nonlinear response is mainly a result of a bandwidth limitation of the counting system. Because of this limitation there is a minimum separation time that is required between two pulses for them to be distinguished. This separation is referred to as the resolving time. The correction we apply is[19]

$$N_{\text{real}} = \frac{N_{\text{meas}}}{1 - N_{\text{meas}}\rho}, \tag{9}$$

where ρ is the resolving time of the discriminator–counter combination, N_{real} is the actual number of photons being detected by the PMT's, and N_{meas} is the number of counts that is registered. This correction assumes that the discriminators perform in an ideal nonparalyzable manner. A nonparalyzable discriminator is one that does not have the dead time that is associated with the response to an initial photon extended by the arrival of a second photon within that initial dead-time region. By contrast a paralyzable discriminator is one that is incapable of registering any output pulses at all above a certain maximum input count rate.[19] The discriminator–counter pair that we use behaves in a manner that is near to this ideal nonparalyzable manner, as we now show.

The resolving-time values that are required for the correction can be empirically determined by comparing a full intensity lidar return profile with a profile that is attenuated through the use of a neutral density filter. N_{real} for each height bin of both profiles is computed by using Eq. (9) for various values of the resolving time. The value that brings the normalized curves into the best agreement is the value that is used in Eq. (9) to correct the nonlinearity of the discriminator–counter circuitry. We assume that the same atmospheric and instrumental conditions prevail during the measurement of both profiles. (A Raman nitrogen filter is used in each channel to acquire these full and reduced intensity data to minimize atmospheric changes.) Figure 3 shows the full and reduced intensity lidar profiles that are normalized to each other between the altitudes of 4 and 10 km. Both profiles are presented with two resolving-time values: ρ = 0, which corresponds to no correction, and ρ = 2.6, which was the value that was chosen for the optimum correction of the data because of the excellent agreement in the corrected curves above 1.6 km. The solid curve that is shown in Fig. 3 is the uncorrected full strength data. The long dashed curve is the full strength data after a resolving-time correction of 2.6 ns has been applied. Likewise the short dashed curve is the uncorrected reduced strength data. The dashed–dotted curve is the reduced strength data after the resolving-time correction has been applied. As a result of these corrections we assume that the shape of the dashed–dotted curve best represents the true nitrogen distribution in the atmosphere since it was acquired at lower intensity and has been corrected for photon overlap. Note in the figure that the resolving-time correction has caused the full strength data to agree with the dashed–dotted curve above 1.6 km. This represents a significant improvement over the uncorrected data that starts to agree with the dashed–dotted curve only above 4 km.

G. Impedance Matching

The output of each of the three PMT's is simultaneously measured by both A/D and PC instruments

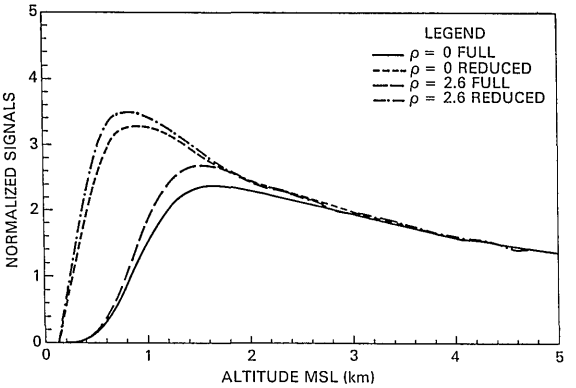

Fig. 3. Water vapor channel data from 4 April 1989 that show the effect of the resolving time correction. Data that are acquired with a 10% neutral density filter in the optical path are normalized and plotted against data that are acquired in a normal full strength manner. The ρ = 0 curves correspond to the uncorrected full and reduced strength data. Note the divergence of the curves below an altitude of ~3 km. The ρ = 2.6 curves show the improved agreement of the data caused by the bandwidth correction. The curves begin to diverge below an altitude of ~1.7 km. These are 10-min data sets.

by simply sending the signals into both instruments in parallel. As the instruments both have input impedances of 50 Ω, this creates an effective 25-Ω load on the PMT. An impedance-matching snubber is used to tune the BNC cable to 25 Ω at the PMT anode, and thereby reflections are suppressed.[20] The snubber also tends to decrease the rise time of the following edge of the (negative going) photo pulse, thus improving the counting characteristics of the PMT.

VI. Analysis

The first data processing that must be done is the application of the resolving-time correction to the PC data. The background is then subtracted from each channel, and a range-squared correction is performed. Since 1988 nearly equal ripple digital filtering[21] of the A/D data has been performed that reduces the basic resolution of 15 to ~150 m. Before 1988 a running seven-point smoothing of the A/D data was performed. The PC data are used with their basic 150-m resolution with no smoothing being performed below 7 km. Above 7 km digital filtering may be used to smooth the PC data as well.

From the A/D and PC measurements of the same 2-min profile we form a single merged profile. Because of the inherently higher quality of the PC data above 2 km, the A/D data are normalized to the PC data. The resulting profile uses A/D data in the first 2 km and PC data above this. This normalization results in a cross-calibration constant for the A/D and PC data. This is a single normalizing constant that produces the best fit of the two data sets. This constant can also be used to determine if the relative sensitivities of the A/D and PC channels change from night to night as is discussed further in Section VII.

The ratios of the signals are next formed by following the analysis that is described by Eqs. (5) and (7). The differential transmission correction and a system self-calibration that are described later are applied. The constants $C_{\mathcal{R},w}$ in Eqs. (5) and (7) must then be determined. In the case of the water vapor mixing ratio, a weighted least-squares fit of the lidar data to a radiosonde water vapor measurement is performed. The aerosol backscattering ratio data on the other hand are calibrated by normalizing to an aerosol-free region of the atmosphere as described in Section III.

To aid in the visualization of the lidar data, all the data profiles from a given night are composited to form a color image that shows the temporal and spatial evolution of the data. A color scale is established by assigning different colors with levels of either the water vapor mixing ratio or aerosol backscattering ratio. Examples of such images are presented in Section VII.

The color images are displayed by using a Matrox QG-640 dual-channel video graphics board interfaced to two NEC Multisync monitors. The QG-640 is capable of displaying two 640- × 480-pixel images in 16 colors simultaneously, which permits side-by-side comparison of related images, as described in Section VII. To create more visually pleasing images the merging height of the A/D and PC data is varied over the image. Instead of choosing a constant height across the image to merge the profiles, the lines of the constant mixing ratio or aerosol backscattering ratio are used in choosing the merging heights.

VII. Results and Calibration

During the period of 6–12 June 1987 the lidar was operated in Greenbelt, Md., on a continuous nighttime basis. Data were also obtained on 11 nights at Otis Air National Guard Base on Cape Cod, Mass. during 23–29 Sept. and 21–24 Oct. 1987. In addition seven nights of data were acquired at Wallops Island, Va., on 10–17 Apr. 1989. During the operational portions of these missions the lidar system functioned properly 97% of the time for a total of nearly 200 h of data. During each of these missions radiosondes were launched at the lidar site. During the Wallops Island mission other moisture sensing instruments including microwave instruments, radar, and sodar were colocated with the lidar.

In this section selected results from these three field measurement programs are presented. In addition examples of calibration methods and the errors associated with the data are described. The water vapor and aerosol data are dealt with in separate subsections.

A. Water Vapor Mixing Ratio Data

Figure 4 shows a typical 2-min profile of background-subtracted, range-squared, and differential transmission-corrected signals for the two Raman and the Rayleigh–Mie A/D returns from 11–12 June 1987. Note the region between 0.1 and 0.8 km where the output beam of the laser is entering the field of view of the telescope. Figure 5 shows the same data as recorded by the PC instruments.

Note the similarity in the major features of Figs. 4 and 5, as expected. Both the water vapor peak between 2 and 3 km and the minimum at 3 km are present in both the A/D and PC data. In addition both A/D and PC aerosol data show a dip at 2 km. Note that the PC data reach their peak between 1 and 2

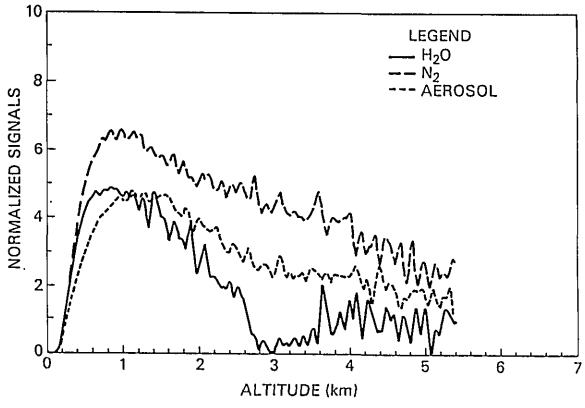

Fig. 4. Two-minute A/D data profiles from the water vapor, nitrogen, and aerosol channels from 7 June 1987. The data have been background subtracted and range-square corrected.

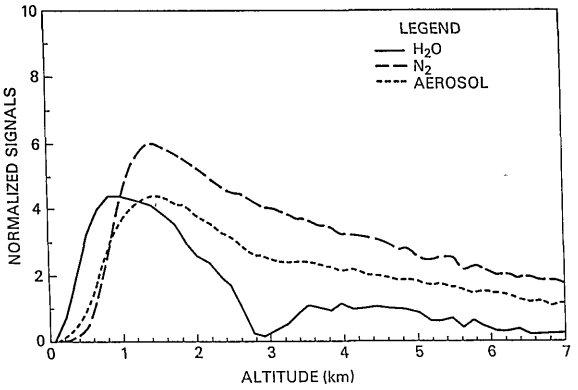

Fig. 5. Two-minute PC data profiles from the same 7 June 1987 time period as in Fig. 4. Note the good overall correspondence of the two data sets. The smoother nature of the PC data is apparent when compared with the A/D data in Fig. 4. Note also the higher altitude range of the PC data.

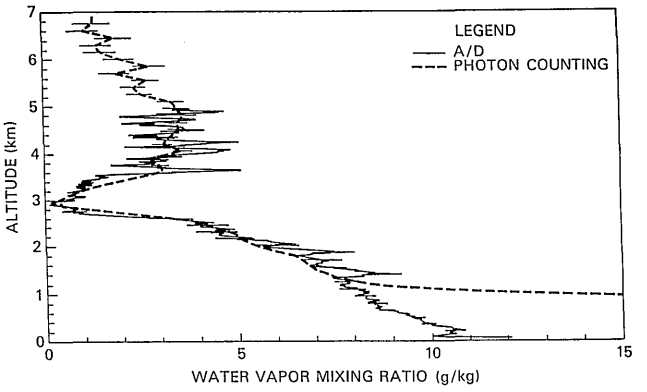

Fig. 6. Two-minute profiles of the water vapor mixing ratio that is calculated from both the A/D and PC data on 7 June 1987. Note the smoother nature of the PC data. Note also that below ~ 1.5 km the PC data are count saturated and diverge from the A/D data.

km. This turn-on time is dominated by the count saturation of the PC channels. Because the channels have different signal intensities, the PC channels achieve their peak signal values at different heights in the atmosphere. The channel that receives the smallest return signal exits the count saturation regime before a channel that receives a larger signal and thus peaks earlier. For example, the water vapor signal, being the weakest, peaks at ~ 1 km. In fact it seems to follow the water vapor A/D data, which indicates that PC saturation may not be a problem in this case of the water vapor channel. On the other hand comparison of the nitrogen A/D and PC signals indicates that the PC data are count saturated up to the peak in the PC data near 1.6 km. The aerosol data also show similar saturation behavior. The nitrogen PC signal on the other hand shows saturation effects up to its peak of ~ 1.6 km. These count saturation effects are coupled with those caused by the geometric overlap of the laser beam and the telescope field of view. It should be noted that the aerosol signal has been attenuated by 3 orders of magnitude by using neutral density filters. Thus comparable signal strengths for all channels are produced.

Figure 6 shows the water vapor mixing ratio as calculated for both the A/D and PC data that are normalized and plotted on the same graph by using data from 7 June 1987. The 1-σ error bars are shown for the PC data. The curves track extremely well with both the A/D and PC instruments by recording the same atmospheric features once the PC instruments are above the count saturation regime, which for this profile is ~ 1.5 km. For the PC ratio profile to be out of saturation, both the water vapor and the nitrogen channels must be unsaturated. Count saturation causes the PC mixing ratio curve to be completely off the graph for heights below 1 km as shown in the figure. The smoother nature of the PC data is also evident from this figure. The A/D data are expected to be noisier because the 200-MHz output of the PMT's is digitized directly as described in Subsection V.B.

A system calibration function is then applied to the data. This calibration corrects for differences in the low-level crossover function for various channels. If no operational parameters are changed on the lidar, the calibration technique also permits a single radiosonde calibration to be used reliably for many nights of data. The small drift in system alignment that may naturally occur from night to night is accounted for by the calibration. The calibration is performed as follows.

At the beginning of each night data are acquired with Raman nitrogen filters in each of the three channels. The H_2O and Rayleigh–Mie channels without their respective bandpass filters have enough leakage at 386.7 nm to allow for reasonable signal strengths in this configuration. The calibration ratios H_2O/N_2 and Rayleigh–Mie/N_2 as functions of height are then formed. The lower 500 m of the ratio profile forms a record of the overlap function for that particular night's alignment. It can therefore be used to calibrate differences in overlap between the channels. In addition the entire ratio profile is a record of how the channel sensitivities compare. Performing this calibration each night compensates for any small changes in channel sensitivities that may occur during a field campaign. This allows a single radiosonde calibration to be tranferred from night to night. A similar technique has been used by Vaughan *et al.*[5] to achieve an absolute calibration of their lidar system.

The calibration method described above was employed for the week-long field mission at Wallops Island in April 1989. The standard deviation of the mean for the PC data calibration constants versus the balloon varied by ±2% for the first five nights. We attribute this change in calibration constant primarily to the optical realignment of the system that was performed each night. Some system changes were made prior to the sixth night of data, which lowered the calibration constant by ~ 10%. Thus, based on these results, the nitrogen filter calibration technique provides a means of transferring the calibration from night to night with errors in the range of

only a few percent provided no changes are made to the operational configuration of the system.

After the calibration correction, a merged A/D and PC profile is formed by taking the A/D data up to ~2 km and by using the PC data above as shown in Fig. 7. The profile is then given in physical units by comparison to a radiosonde measurement. Figure 7 shows lidar data from 7 June 1987 compared with a contemporaneous radiosonde by using a single calibration constant. In general Fig. 7 shows excellent agreement between the lidar and the balloon. There are, however, two regions of disagreement.

The first of these is the low-level disagreement between the surface and ~300–400 m, which can be attributed to different crossover functions for H_2O and N_2 channels. For a perfectly designed and aligned optical system, the ratio data should still be valid within this overlap region since they would have the same overlap function. If, however, the overlap function is not the same for the two channels that are used in the ratio, the ratio will have a nonlinear behavior in this overlap region. The calibration technique described above corrects for these differences. These data have an overlap problem in this region because they were taken before we began using the nitrogen filter calibration technique. We first tested this calibration technique during the September–October 1987 mission but did not begin to implement it rigorously until Apr. 1989.

The second region of disagreement between the lidar and the balloon measurement occurs around 3 km. This disagreement is due to the inability of the standard moisture sensing element (the carbon hygristor) that is used in the radiosondes to measure moisture reliably below a RH of ~20%. Note that the lidar indicates a mixing ratio below 0.5 g/kg, while the balloon indicates ~1.5 g/kg. This 1.5-g/kg level is close to the 20% RH line, which has been plotted for reference. This radiosonde limitation is addressed much more fully by Melfi *et al.*[6] The error bars that denote the standard deviation of the data for the derived mixing ratio are also plotted. Note that the error at 7 km is ±0.7 g/kg, which, as a result of the small values being measured, amounts to a ±30% random error. For the measurements at 5 km, however, the error is at most ±10% and is smaller at lower altitudes.

As described in Section VI color composite images are formed by using all profiles from a single night, such as that in Fig. 7. The color composite images for the night of 7 June 1987 have been made and were found to be similar to ones that have been previously presented in Refs. 6 and 18. By contrast, perhaps the most meteorologically interesting data that we have acquired with the system were taken on 29–30 September 1987 at Cape Cod, Mass. We have therefore chosen to present the color images from that night. Plate 8 shows the water vapor mixing ratio as a function of height and time during the night of 29–30 September 1987 that was derived from our lidar measurements. The vertical scale represents the altitude from the surface to nearly 7 km. The horizontal scale represents time with measurements that begin before 2000 EDT and extend to almost 0600 EDT the next morning, which is more than 10 continuous hours of lidar data. The water vapor mixing ratio is color coded by intensity with the color bar shown on the right. The color scale progresses from black and dark blue for values with a mixing ratio of 0–1 g/kg to red and violet for values of 10–12 g/kg. This image is analyzed in its synoptic context after the presentation of the aerosol backscatter ratio data. It should be noted that the vertical striping in the upper right of the image is not meteorological in origin but is instead a result of attenuation of the laser beam by clouds.

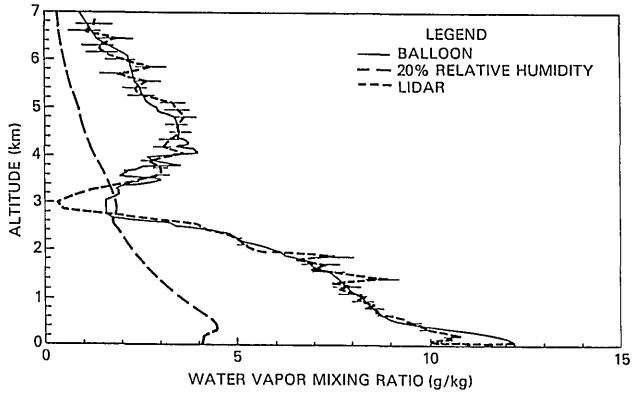

Fig. 7. Composite 2-min lidar water vapor mixing ratio profile from 7 June 1987 compared with a colocated radiosonde. The A/D and PC lidar data profiles have been joined at ~2 km. Note the overall good agreement except at 3 km, where the radiosonde is incapable of properly measuring moisture in regions where the RH is below ~20%.

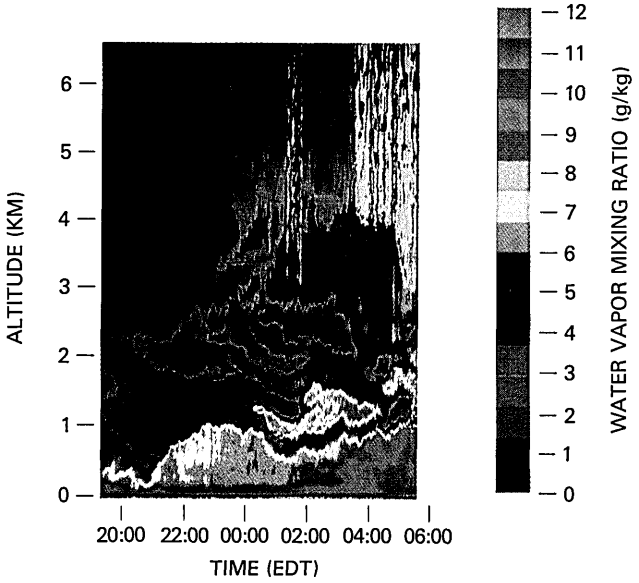

Fig. 8. Composite image of the water vapor mixing ratio that is derived from lidar measurements that were made during the night of 29–30 Sept. 1987. The vertical scale represents the altitude from the surface to nearly 7 km. The horizontal scale represents the time with measurements beginning before 2000 EDT and extending to almost 0600 EDT the next morning.

B. Aerosol Backscattering Ratio Data

The combined A/D and PC profile of the aerosol backscattering ratio is formed in a similar fashion to that of the water vapor mixing ratio data. The aerosol backscattering ratio system calibration constant is determined by assuming that there is an essentially aerosol-free region within the data set. The assumption is thus made that somewhere between the heights of 4 and 7 km there is a region where the aerosol backscattering ratio is at a minimum and thus can be set to unity, which indicates only molecular scattering. The height of the aerosol-free region is determined by choosing the minimum of the aerosol backscattering ratio curve in the 4–7-km range. The choice of 7 km as the upper limit in the search for an aerosol-free region is dictated by signal-to-noise constraints.

An example of a lidar-derived aerosol backscattering ratio is given in Fig. 9 from data taken during the night of 7 June 1987. Between 4 and 7 km the minimum scattering is seen to be at ~6.9 km. The profile is rescaled by normalizing the data at this height to unity as described in Section III. The nitrogen calibration correction has not been applied to these data, which explains the values of the backscattering ratio below $\mathscr{R} = 1$ from the ground up to ~0.5 km. Note the aerosol peak at ~1.6 km where the backscattering ratio approaches 1.4. This indicates aerosol scattering that is 40% as large as the pure molecular scattering at this height. This high backscattering ratio is probably associated with the high moisture that is present at this height. Just above this peak, at 3 km, the backscattering ratio is only slightly greater than 1.0, which indicates that the atmosphere is almost free of aerosols at this height. The magnitude of the random error for the aerosol backscattering ratio is much greater than for the water vapor mixing ratio, which reaches 50–100% around 7 km. This is due to the very low amounts of aerosols that are present at this level.

As mentioned above in our analysis the assumption is made that the minimum region of backscattering in the data is at a height that is completely free of aerosols. There is potentially a very small error that is introduced by this assumption. Russell *et al.*[22,23] state that indeed the free troposphere in nonvolcanic conditions is usually quite free of aerosols but that the assumption that it is completely aerosol free can produce some errors. They show that the assumed minimum backscattering ratio in the mid-latitudes at a wavelength of 690 nm should be $\mathscr{R}_{min} = 1.02$ instead of the completely aerosol-free assumption of $\mathscr{R}_{min} = 1.00$. Using this $\mathscr{R}_{min}$ value and a λ^{-4} wavelength dependence of Rayleigh scattering and assuming a λ^{-1} dependence for the aerosol backscattering coefficient[16] implies that at 354.7 nm $\mathscr{R}_{min}$ should be ~1.002. We neglect the possibility of this small error in the analysis.

As in the case for the water vapor data, composite color images of aerosol backscattering ratio data are formed to aid visualization of the aerosol field. The spatial and temporal evolution of aerosols is seen quite well in the composite color image of Fig. 10. The color bar that is used with the image progresses from black to dark blue for backscattering ratios near 1.0 to red and purple for values of backscattering between 3 and 4. This image is described in its meteorological context in Subsection VII.C.

C. 29–30 Sept. 1987

As we mentioned above, the Raman lidar was stationed at Otis Air National Guard Base on Cape Cod, Mass., during most of September and October in 1987. The surface chart for 0000 UTC on 30 Sept. 1987 is shown in Fig. 11. The chart shows that at 0000 UTC a low-pressure system was centered north of Ottawa. The cold front that was associated with it stretched to the southeast through central Tennessee and toward the Gulf of Mexico. The corresponding warm front stretched generally eastward from the low to northern Newfoundland. There was also a stationary front that was situated over the Atlantic

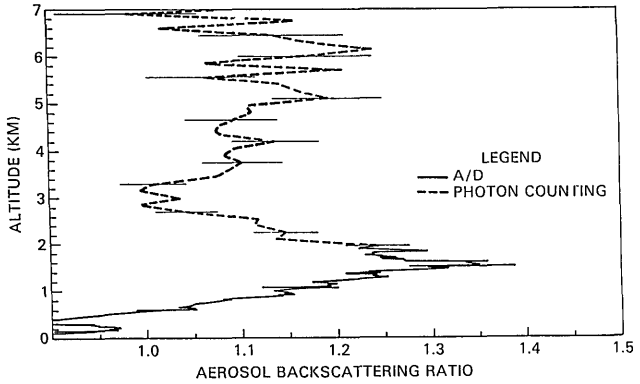

Fig. 9. Composite aerosol backscattering ratio profile from 7 June 1987. The values of a backscattering ratio of less than 1.0 in the region below 500 m are caused by nonlinear crossover effects (see text).

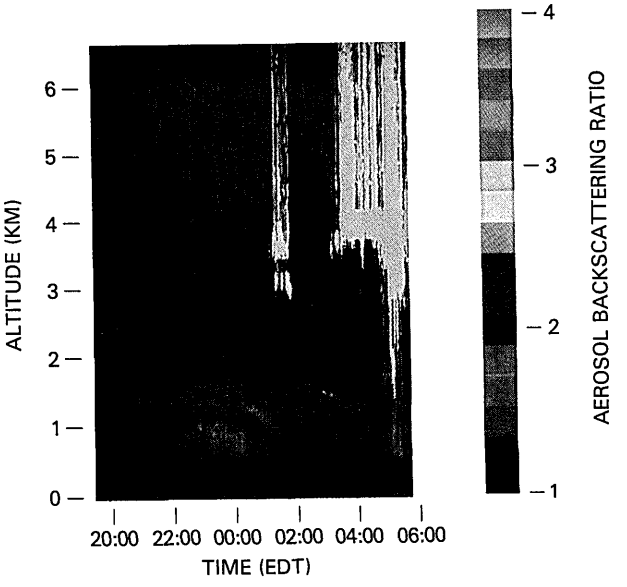

Fig. 10. Composite image of the lidar-derived aerosol backscattering ratio during the night of 29–30 September 1987.

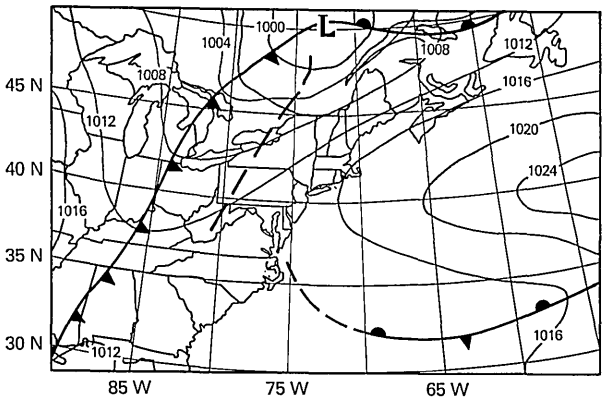

Fig. 11. The 0000 UTC surface chart on 30 Sept. 1987.

between 30° and 35° N. The tail of this stationary front curved on a northwestward track toward the Chesapeake Bay region of the mid-Atlantic coast. The lines of constant pressure (isobars) shown indicate that the central pressure of the low was less than 1000 mbars and that the pressure was increasing both toward the southeast and toward the southwest. Winds generally flow counterclockwise around a region of low pressure, and they tend to follow the isobar contours. This indicates that the winds over the Cape Cod region were out of the south. This southerly flow persisted for the entire evening and produced a warming trend and an increase in moisture over the course of the night at the lidar site.

Figure 8 shows this increase in moisture at all levels during the course of the evening. The black and dark blue regions (0–2 g/kg) at the beginning of the night are replaced by greens, yellows, and reds (5–10 g/kg) by the end. With the increase in moisture came the breakout of a cloud ceiling at ~4 km just before 0400 EDT. Some small clouds are indicated by the noisy striping seen at ~0130 with bases at ~3 km. A much larger group of clouds is indicated by the purple lines with bases between 4 and 5 km between 0400 and 0600 EDT. When the laser is blocked by thick clouds such as this latter set, no meaningful measurements are possible above them. This explains the noisy nature of the image above the base of these clouds. If the clouds are either thin or do not form a continuous layer as in the first set, it is possible to receive a sufficient return from the overlying atmosphere to obtain some idea of the moisture structure there. The cloud ceiling can be seen to be lowering from 0400 to 0600 EDT by which time rain was reaching the surface, which necessitated shutdown of the lidar.

Figure 8 is striking for the extreme gradients of moisture that are present throughout the image. Note, for example, the dark blue region at 1.2 km at ~0500 EDT. Within just 30 min temporally and a few hundred meters vertically, the mixing ratio changes by approximately an order of magnitude from ~1 g/kg to nearly 10 g/kg. Numerous other areas of high-moisture gradient can be found in the image.

The gradient of moisture affects cloud formation processes and influences atmospheric stability. The standard radiosonde instruments that are used for moisture measurements are not capable of capturing the spatial and temporal variability that is present in this image. Even if they were launched in rapid succession at a single site, the balloons drift with the wind, which makes it impossible to sample repetitively the same geometric volume as is possible with the lidar. In addition, as mentioned earlier, the standard radiosonde has difficulty making accurate water vapor measurements in conditions of low RH.[5]

Measurements of pressure and temperature from the radiosondes that are launched during the night were combined with the lidar mixing ratio data to compute the RH over the course of the evening of 29–30 September. This is shown in Fig. 12. The ability of a given mass of air to contain water vapor increases with temperature; i.e., the saturation mixing ratio (mixing ratio for 100% RH) increases with temperature. Thus the images in Figs. 8 and 12 will have different appearances because the water vapor mixing ratio that corresponds to a certain RH varies with the temperature. The temperature as reported by the radiosondes increased throughout the night. This can also be inferred from the images. Compare the RH at 0.8 km first at 2300 EDT and then at 0400 EDT. In both these regions the RH is in the 70–90% range. However, in the first case the corresponding mixing ratio is ~7–8 g/kg, while in the second it is ~10 g/kg. In addition the large region of moisture between 0000 and 0500 EDT at heights of 3–5 km is generally in the 70–90% RH range. On the other hand the water vapor image shows values of a mixing ratio that varies by a factor of 2 between ~3 and 6 g/kg. This vertical and temporal structure of the RH is important for understanding the growth of aerosols and cloud formation.

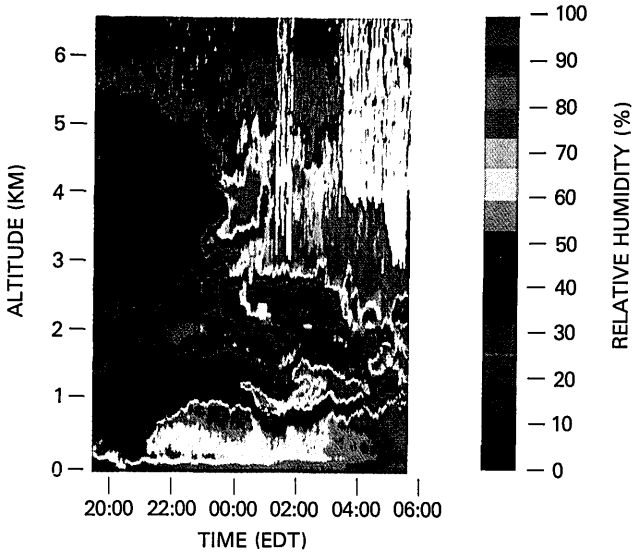

Fig. 12. Composite image of RH during the night of 29–30 September 1987 that is derived from lidar measurements of the water vapor mixing ratio and radiosonde measurements of pressure and temperature. The horizontal and vertical scales are the same as in Fig. 1.

There is a general correspondence between high RH and the growth of aerosols.[24] This correspondence can be seen in the lidar data. Compare the RH image in Fig. 12 with the aerosol backscattering ratio image in Fig. 10. Focus on the region between 2200 and 0100 EDT between 800 and 1000 m. The aerosol backscattering ratio values are in the range of 1.6–1.8 in this region. This indicates that in this region the amount of scattering at the laser wavelength caused by particles is 0.6–0.8 times the scattering caused by air molecules alone. The corresponding RH is in the 80–90% range. This same relationship of the backscattering ratio to RH holds for the aerosol peak at the same height at 0500 EDT. However, it should also be noted that the high aerosol backscattering ratio need not be correlated with the high RH. Different air masses can intermingle and produce both dry and moist aerosol-laden regions in close proximity. For example, a significant amount of aerosols is present in the region between 2100 and 0000 EDT at 1–5 km where the RH is 10–20%. This is very close to the region that is mentioned earlier at 0000 EDT and 1 km where both the moisture and aerosol content are high. It is also interesting to note the line of high scattering ratio at ~0500 EDT extending from the cloud base down to ~1.3 km. This could well indicate the presence of virga (falling rain that does not reach the ground). As noted earlier shortly thereafter rain reached the surface and necessitated the shutdown of the lidar.

Some features of Fig. 10 that are thought to not be atmospheric in nature should be pointed out. The point at which the A/D and PC data are joined can be seen at around 1.6 km. The region below 1.6 km shows finer stipling caused by the higher sampling rate of the A/D instruments. Above 1.6 km the smoother nature of the PC data can be seen easily. The second feature to note is the vertical striping on the left side of the image, which is probably due to small amounts of background that were not removed in the data processing. Subtraction of the background is particularly difficult in this aerosol case because of the very small amounts of aerosols being measured. And finally Fig. 10 shows an increase in the scattering ratio above 4 km. This is thought to be caused by small amounts of afterpulsing in the aerosol channel PMT. We are currently working on a calibration technique for this problem.

VIII. Other Analyses

The type of analysis that has been presented here by using the lidar data is greatly expanded by Melfi *et al.*[5] in the treatment of warm and cold fronts by using the data from June 1987 taken at Greenbelt, Md. The various other types of measurement and analysis that use the Raman lidar data that have also been performed include the following:

(1) Assessment of spatial and temporal scales of atmospheric moisture variance.

(2) Calculation of the static, dynamic, and convective stability of the atmosphere.

(3) Moisture measurements up to the height of the tropopause.

(4) Aerosol backscattering and extinction coefficients and their relationship to each other and to moisture.

(5) Observation of gravity waves.

IX. Summary and Conclusions

In over 200 h of data acquisition during several field campaigns, the Raman lidar has shown itself to be a reliable, valuable tool for the study of water vapor and aerosols in the lower atmosphere. Building an instrument that is capable of this level of performance has required several years of effort. The equipment that was used to do that and many of the problems that were solved in the process have been presented. Two-minute profiles of the water vapor mixing ratio and aerosol backscattering ratio from the surface to 7 km have also been presented. These profiles were then composited to form color images to aid in the visualization of the temporal and spatial variation of both the moisture and aerosol fields. The analysis of these images has shown that the variability in the moisture field exists on scales that are not being measured, and perhaps cannot possibly be measured, by the radiosonde that is the standard moisture measuring tool of the meteorological community.

The authors wish to recognize Glenn Staley, Max Strange, Pete Leone, Luis Ramos-Izquierdo, Ken Kirks, Ray DiSilvestre, Susan Hill, Dick Aldridge, Lou Shelton, and Jim Marsh for their contributions to the development of the lidar system. In addition we thank Frank Schmidlin, Jim Morrisey, Clyde Lawrence, Ralph Hoar, Riley Bull, Sam Duffee, and Sam West for providing radiosonde launch support. We also thank Bill Grant of NASA/Langley Research Center for helpful comments on the manuscript. The mention of a particular product or manufacturer should not be construed as an endorsement of that product or manufacturer by NASA/Goddard Space Flight Center.

References

1. J. A. Cooney, "Remote measurements of atmospheric water vapor profiles using the Raman component of laser backscatter," J. Appl. Meteorol. **9,** 182–184 (1970).
2. S. H. Melfi, J. D. Lawrence, Jr., and M. P. McCormick, "Observation of Raman scattering by water vapor in the atmosphere," Appl. Phys. Lett. **15,** 295–297 (1969).
3. J. C. Pourney, D. Renaut, and A. Orszag, "Raman-lidar humidity sounding of the atmospheric boundary layer," Appl. Opt. **18,** 1141–1148 (1979).
4. S. H. Melfi and D. Whiteman, "Observation of lower-atmospheric moisture structure and its evolution using a Raman lidar," Bull. Am. Meteorol. Soc. **66,** 1288–1292 (1985).
5. G. Vaughan, D. P. Wareing, L. Thomas, and V. Mitev, "Humidity measurements in the free troposphere using Raman backscatter," Q. J. R. Meteorol. Soc. **114,** 1471–1484 (1988).
6. S. H. Melfi, D. Whiteman, and R. Ferrare, "Observation of atmospheric fronts using Raman lidar moisture measurements," J. Appl. Meteorol. **28,** 789–806 (1989).
7. C. E. Junge and J. E. Manson, "Stratospheric aerosol studies," J. Geophys. Res. **66,** 2163–2182 (1961).

8. G. Fiocco and G. Grams, "Observations of the aerosol layer at 20 km by optical radar," J. Atmos. Sci. **21,** 323–324 (1964).
9. J. D. Spinhirne, W. D. Hart, and R. Boers, "Cloud top liquid water from lidar observations of marine stratocumulus," J. Appl. Meteorol. **28,** 81–90 (1989).
10. R. Boers, J. D. Spinhirne, and W. Hart, "Lidar observations of the fine-scale variability of marine stratocumulus clouds," J. Appl. Meteorol. **27,** 797–810 (1988).
11. H. Inaba, "Detection of atoms and molecules by Raman scattering and resonance fluorescence," in *Laser Monitoring of the Atmosphere,* E. D. Hinkley, ed. (Springer-Verlag, Berlin, 1976).
12. H. Inaba and T. Kobayasi, "Laser Raman radar–laser Raman scattering methods for remote detection and analysis of atmospheric pollution," Optoelectronics **4,** 101–123 (1972).
13. J. L. Bribes, R. Gaufres, M. Monan, M. Lapp, and C. M. Penney, "Raman band contours for water vapor as a function of temperature," Appl. Phys. Lett. **28**(6), 336–337 (1976).
14. C. M. Penney and M. Lapp, "Raman-scattering cross sections for water vapor," J. Opt. Soc. Am. **66,** 422–425 (1976).
15. R. M. Measures, *Laser Remote Sensing Fundamentals and Applications* (Wiley, New York, 1984), p. 108.
16. E. P. Shettle and R. W. Fenn, *Models of the Atmospheric Aerosols and Their Optical Properties,* AGARD Proc. **183** (1976).
17. S. E. Koch, P. B. Dorian, R. Ferrare, S. H. Melfi, W. C. Skillman, and D. Whiteman, "Structure of an internal bore and dissipating gravity current as revealed by Raman lidar," Mon. Weather Rev. **119,** 857–887 (1991).
18. R. W. Hamming, *Digital Filters* (Prentice-Hall, Englewood Cliffs, N.J., 1989), p. 22.
19. R. D. Evans, *The Atomic Nucleus* (McGraw-Hill, New York, 1955), p. 785.
20. *SR 400 Manual* (Stanford Research Systems, Inc., Sunnyvale, Calif., 1987).
21. J. F. Kaiser and W. A. Reed, "Data smoothing using low-pass digital filters," Rev. Sci. Instrum. **48,** 1447–1457 (1977).
22. P. B. Russell, T. J. Swissler, and M. P. McCormick, "Methodology for error analysis and simulation of lidar measurements," Appl. Opt. **18,** 3783–3797 (1979).
23. P. B. Russell, B. M. Morley, J. M. Livingston, G. W. Grams, and E. M. Patterson, "Orbiting lidar simulations. 1: Aerosol and cloud measurements by an independent-wavelength technique," Appl. Opt. **21,** 1541–1553 (1982).
24. J. W. Fitzgerald and W. A. Hoppel, "Equilibrium size of atmospheric aerosol particles as a function of relative humidity: calculations based on measured aerosol properties," in *Hygroscopic Aerosols,* L. Ruhnke and A. Deepak, eds. (A. Deepak, Hampton, Va., 1984), p. 2.